Geochemistry, Geophysics, Geosystems

RESEARCH ARTICLE

10.1029/2023GC011043

Machine Learning-Based New Earthquake Catalog Illuminates On-Fault and Off-Fault Seismicity Patterns at the Discovery Transform Fault, East Pacific Rise

Jianhua Gong[1,2], **Wenyuan Fan**[1], **and Ross Parnell-Turner**[1]

[1]Scripps Institution of Oceanography, UCSD, La Jolla, CA, USA, [2]Indiana University Bloomington, Bloomington, IN, USA

Key Points:

- The western Discovery transform fault has seven patches that are likely dominated by alternating seismic and aseismic slip modes
- Machine-learning method helps to identify off-fault seismicity along abyssal hills, indicating ongoing deformation within the oceanic plate
- The Discovery transform system is young and still evolving, forming an interactive system with faulting, rifting, and plate rotation

Supporting Information:

Supporting Information may be found in the online version of this article.

Correspondence to:

J. Gong,
gongjian@iu.edu

Citation:

Gong, J., Fan, W., & Parnell-Turner, R. (2023). Machine learning-based new earthquake catalog illuminates on-fault and off-fault seismicity patterns at the Discovery transform fault, East Pacific Rise. *Geochemistry, Geophysics, Geosystems*, *24*, e2023GC011043. https://doi.org/10.1029/2023GC011043

Received 10 MAY 2023
Accepted 18 AUG 2023

Author Contributions:

Conceptualization: Wenyuan Fan
Formal analysis: Jianhua Gong, Wenyuan Fan, Ross Parnell-Turner
Funding acquisition: Wenyuan Fan
Methodology: Jianhua Gong, Wenyuan Fan
Supervision: Wenyuan Fan
Writing – original draft: Jianhua Gong, Wenyuan Fan

Abstract Oceanic transform faults connect spreading centers and are imprinted with previous tectonic events. However, their tectonic interactions are not well understood due to limited observations. The Discovery transform fault system at 4°S, East Pacific Rise (EPR), represents a young transform system, offering a unique opportunity to study the interplay between faulting and other tectonic events at an early phases of an oceanic transform system. Discovery regularly hosts $M5$–6 characteristic earthquakes, and the seafloor north of Discovery includes a 35 km-long rift zone that records a complex history of rifting, faulting and volcanism, suggesting that the transform faults likely interact with regional tectonic activity. We apply a machine-learning enabled workflow to locate 21,391 earthquakes recorded during a 1-year ocean bottom seismometer experiment in 2008. Our results indicate that seismicity on the western Discovery fault is separated into seven patches with distinct aseismic and seismic slip modes. Additionally, we observe a patch of off-fault seismicity near where seafloor abyssal hills intersect the rift zone. This seismicity may have been caused by varying opening rates as spreading rate decreases from north to south in the rift zone. Our findings suggest that the Discovery system is still evolving, and that system equilibrium has not been reached between rifting and faulting. These results reflect the complex yet rarely observed interactions between fault slip, plate rotation, and rifting which are likely ubiquitous at oceanic transform systems.

Plain Language Summary Oceanic transform faults are major plate boundaries connecting mid-ocean ridges. Despite their important role in plate tectonics, their interactions with adjacent mid-ocean ridges and surrounding oceanic plates are not well understood. The Discovery transform fault system at 4°S, East Pacific Rise, is a young oceanic transform system formed approximately 1 My ago, offering a unique opportunity to study the interplay between faulting and other tectonic events at an early phase of an OTF. Discovery faults have quasi-periodical magnitude (M) 5–6 earthquakes. Using ocean bottom seismometer data recorded over 1 year, we find that seismicity of the western Discovery fault can be grouped into seven patches, indicating division of alternating slip modes that either releases tectonic strain by $M > 5$ earthquakes or creep steadily. North of the western Discovery fault, a ~10 km wide rift zone, abundant seamounts, and abyssal hills form an interactive tectonic complex. We observe a patch of off-fault seismicity coinciding with seafloor abyssal hills near their intersection with the rift zone. This off-fault seismicity indicates ongoing deformation within the oceanic plate and possible spatial variations in rifting rates. Our results suggest that the Discovery system is still evolving with rifting and faulting accommodating plate spreading simultaneously.

1. Introduction

Oceanic transform faults (OTFs) are strike-slip faults with nearly vertical fault planes. In conjunction with the orientations of their fracture zones (FZ), OTF strike directions are indicative of both present and past spreading directions (DeMets et al., 2010). Despite their seemingly simple structure and motion, OTFs exhibit perplexing fault slip behaviors, with the majority of slip released aseismically (Boettcher & Jordan, 2004). Moreover, large earthquakes repeatedly rupture the same fault patches, generating characteristic earthquakes (McGuire, 2008; Shi et al., 2021). Several mechanisms have been proposed to explain seismic and aseismic partitioning of OTFs, including along-strike variations in frictional properties (Y. Liu et al., 2020), crust-mantle interactions (Kuna et al., 2019), deep fluid circulation (Kohli et al., 2021; Roland et al., 2012; Yu et al., 2021), and variations in fault structure due to microplate formation (Wolfson-Schwehr et al., 2014) or rotation (Gong et al., 2022; Ren et al., 2023). Collectively, these mechanisms reflect the feedback between fault slip, local plate motion, fault architecture, and fluid and magma fluxes within OTF systems.

Writing – review & editing: Jianhua Gong, Wenyuan Fan, Ross Parnell-Turner

The Quebrada-Discovery-Gofar transforms are three successive OTF systems along the East Pacific Rise (EPR) south of the equator, with a full spreading rate of ∼140 mm/yr (Figure 1a; Dunn, 2015). Despite their close proximity, the three transform systems exhibit considerable differences in seafloor geomorphology and fault slip behavior (Pickle et al., 2009; Searle, 1983). Both Quebrada and Gofar have FZ extending approximately 370 km to the Bauer and Anti-Bauer scarps (Goff & Cochran, 1996), while Discovery has less obvious FZ (Mammerickx et al., 1975; Searle et al., 1981), suggesting that the Discovery system was formed later than the other two systems. Further differences between the OTF systems include that the Quebrada transform faults are situated in deep valleys, while the Gofar and Discovery systems have shallower bathymetry. Additionally, Quebrada likely has approximately 4 km-thick oceanic crust, while the other two systems likely have more typical, 6 km-thick oceanic crust (Pickle et al., 2009; Roland et al., 2012). Intriguingly, Gofar and Discovery host quasi-periodic magnitude (*M*) 5 to 6 earthquakes on several distinct fault patches, while Quebrada seldom hosts events with magnitude greater than 5 (McGuire et al., 2012; Shi et al., 2021; Wolfson-Schwehr et al., 2014). These differences between the three nearby OTFs indicate that local plate tectonic processes can strongly influence the structure and seismic behaviors of OTFs.

The Discovery transform fault system consists two fault strands, D1 and D2, connected by a ∼5 km long intra-transform spreading center (ITSC; Figure 1b). Both D1 and D2 have *M*5–6 earthquakes every 5–6 years (Shi et al., 2021; Wolfson-Schwehr & Boettcher, 2019; Wolfson-Schwehr et al., 2014). The seafloor morphology north of Discovery shows fragmented relief, suggesting a complex tectonic evolution that likely influenced the formation of the Discovery transform fault and seismic activity (Wolfson-Schwehr et al., 2014). Ocean bottom seismometer (OBS) data was collected along the Discovery transform fault in 2008 during the Quebrada-Discovery-Gofar experiment to study seismicity and fault properties of the OTF systems (Figure 1). For example, Wolfson-Schwehr et al. (2014) used the short-term average/long-term average (STA/LTA) and wavelet methods to detect *P* and *S* arrivals to locate microseismicity along Discovery. However, the *P* wave amplitudes of the OTF earthquakes are much smaller due to the marine environment, posing challenges to identify *P* waves using the conventional STA/LTA method.

In this study, we present a new workflow for earthquake detection, location, and relocation using efficient machine learning methods and waveform cross-correlation data that are advantageous in processing OBS data compared to standard approaches. We aim to identify inter-relationships between seismicity, fault structure, and local tectonics at the Discovery system. We find that the western Discovery strand (D2) may have segmented into seven patches with distinct seismicity features. We also identify a seismicity gap zone that may have been caused by a small-scale, off-ridge rift within the Discovery system. This rift causes off-fault seismicity and may still be an active tectonic event that continues to influence local tectonics and seismicity.

2. Data

The 2008 Quebrada-Discovery-Gofar experiment aimed to investigate the seismogenic properties of EPR transform faults by deploying an array of 30 broadband seismometers and 10 short period seismometers (McGuire et al., 2012). The experiment successfully recorded abundant microseismicity along the transform faults and captured an anticipated M6 earthquake that occurred on 18 September 2008, at the westernmost Gofar transform faults (G3, Figure 1a). Along the western (D2) strand of the Discovery transform fault (Figure 1b), eight broadband seismometers were deployed at depths ranging from 2680 to 3,270 m below the sea surface, including two situated in the transform fault valley. The stations were configured to record ground motions at sampling rates of 50 or 100 Hz (Table S1 in Supporting Information S1). All the seismometers at Discovery operated as intended and were successfully recovered after the experiment.

3. Methods

Microseismicity provides valuable insights into the fault structure, slip mode, and tectonic processes at OTFs (e.g., Gong & Fan, 2022; Gong et al., 2022; Kuna et al., 2019; McGuire et al., 2012; Ren et al., 2023; Wolfson-Schwehr et al., 2014; Yu et al., 2021). We introduce a new workflow for detecting and locating microearthquakes using machine learning techniques. The earthquakes are further relocated using cross-correlation data of *P* and *S* waves.

We use a machine learning phase picker, PhaseNet (Zhu & Beroza, 2018), to detect *P* and *S* phases. To account for the shorter *S*-*P* times of the Discovery earthquakes compared to those used in the PhaseNet training data set,

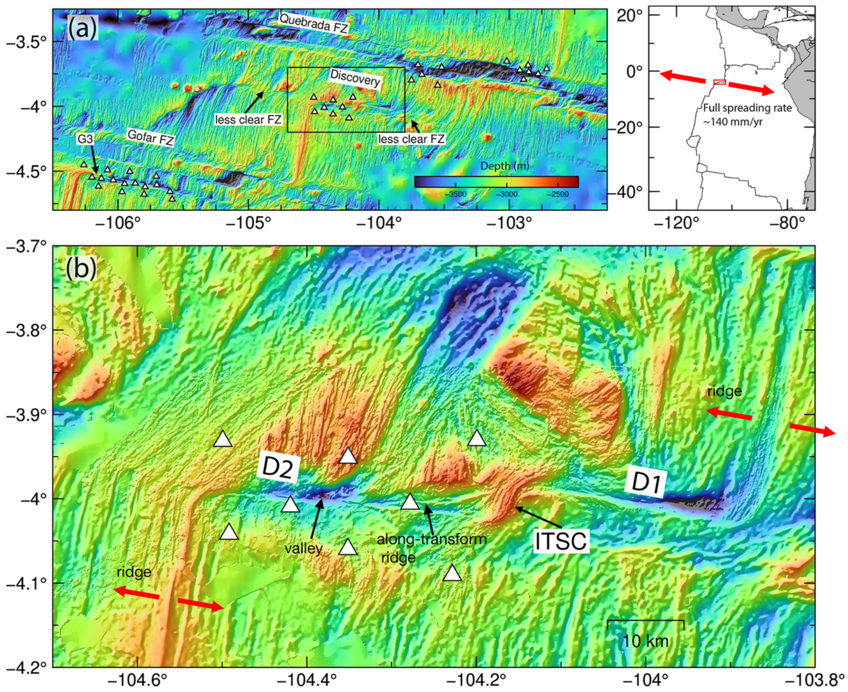

Figure 1. Map of study area. (a) Bathymetry of the Quebrada-Discovery-Gofar transform systems (left panel) and a zoom-out view of the study area (right panel). Well-defined fracture zones are visible for Quebrada and Gofar transform faults, while those at Discovery are less distinct. White triangles denote ocean bottom seismometers; red box in the zoom-out view panel indicates the map area in the left panel; black lines are plate boundaries; red arrows denote spreading direction. (b) Bathymetry around Discovery transform faults. D1 and D2 denote the eastern and western segments of Discovery transform fault. Mid-ocean ridge (ridge) and inter-transform spreading center are labeled.

we upsample the data prior to applying the PhaseNet algorithm (e.g., Gong et al., 2022; Gong & Fan, 2022). We test upsampling factors of 1–4 on a 1 month long subset of waveform data for all stations and find that an upsampling factor of 4 yields the most *P* and *S* detections (Figure S1 in Supporting Information S1). Additionally, we compare the performance of PhaseNet to another machine-learning phase picker, EQTransformer (Mousavi et al., 2020), on our OBS data, and observe that PhaseNet systematically outperforms EQTransformer when the upsampling factor is greater than 1. In total, we detect 3,507,920 *P* arrivals and 4,858,299 *S* arrivals.

We then associate *P* and *S* phase picks using open-source program GaMMA (Zhu et al., 2022). GaMMA models the collection of phase picks of an event using the multivariate Gaussian distribution, and outputs associated phase picks of an event as well as rough estimates of its origin time and location. The detailed input parameters for GaMMA are provided in Table S2 in Supporting Information S1. Only events with at least eight combined phase picks, including both *P* and *S* picks, are retained, resulting 23,495 candidate earthquakes.

To locate and relocate the seismicity and compute their local magnitude, we follow the workflow of Gong et al. (2022). We use COMPLOC (Lin & Shearer, 2006) to locate each earthquake with the associated *P*- and *S*-wave arrival times computed using one-dimensional *P* and *S* velocity profiles from Roland et al. (2012) (Figure S2 in Supporting Information S1). The COMPLOC location procedure is conducted iteratively 20 times and events within 1 km depth to the seafloor are removed after each iteration, resulting 21,404 initially locatable events (Figures S3 and S4 in Supporting Information S1). Initial earthquake locations are further refined through relocation using GrowClust (Matoza et al., 2013; Trugman & Shearer, 2017). We apply this method to cross-correlation data of body waveforms to obtain high-precision relative earthquake locations. Location uncertainties related to COMPLOC and GrowClust are discussed in more details in Gong and Fan (2022), which applied a similar workflow to locate seismicity along Gofar transform fault, and therefore are not repeated here. The eight OBS stations provide a good coverage for D2 and a minimum of eight P plus S picks for each event ensures a good location constrain. In total, we successfully relocate 21,391 earthquakes (Figure 2).

For the relocated earthquakes, we compute local magnitudes (M_L) using three-component displacement waveforms, following Gong et al. (2022). Seismic records are converted to the Wood-Anderson instrument response,

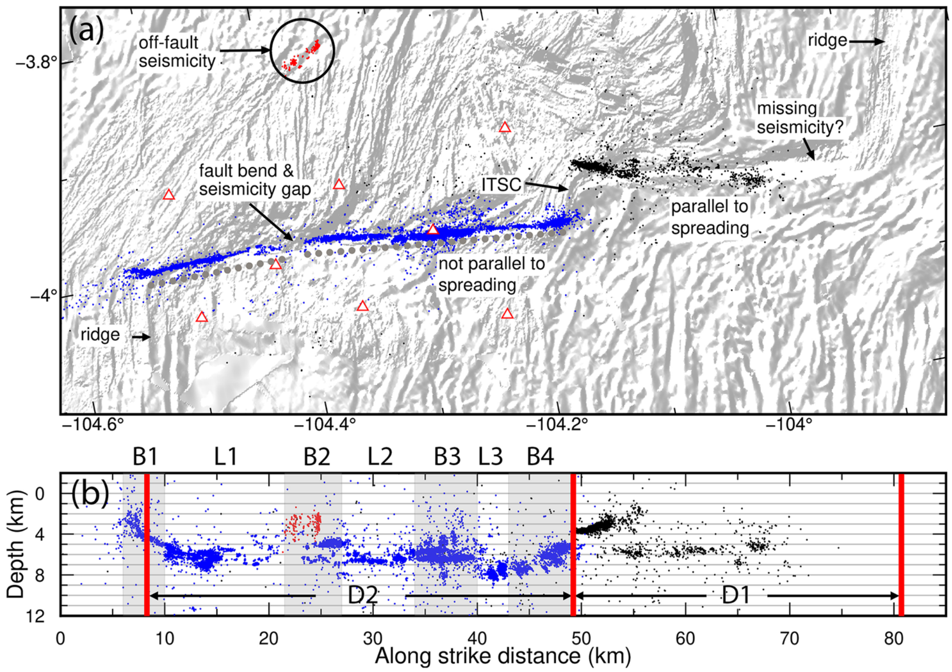

Figure 2. (a) Relocated earthquakes plotted in oblique Mercator projection, using Nazca-Pacific rotation pole 88.6°W/52.7°N as the projection pole (DeMets et al., 2010), and 104.2°W/3.95°S as the projection center. Black, blue and red dots represent earthquakes occurring along D1, along D2, and within the oceanic plate, respectively; gray dotted lines are interpreted orientations of D2 fault traces (this study), which are not parallel with the plate spreading direction from the kinematic plate motion model (DeMets et al., 2010). (b) Depth cross-section. Red vertical lines denote the locations of ridges and ITSC; B1 to B4 and L1 to L3 denote the alteration of barrier and locked zones along D2, with the gray shaded areas indicating the barrier zones (B1–B4).

filtered between 4 and 20 Hz, and windowed from 1 s before to 5 s after the predicted *S* arrivals. We calculate a peak amplitude (A) as the maximum root sum square of the windowed displacements and measure the peak noise amplitude (A_N) using the same approach on a 2–5 s window before the predicted *P* arrivals. A local magnitude estimate M_L is recorded at a given station if the signal to noise ratio (A/A_N) is greater than 10, and M_L is computed as

$$M_L = \log_{10} A + 2.56 \log_{10} D - 1.67, \tag{1}$$

where D is the hypocentral distance (Shearer, 2019). The final M_L is estimated as the median value of M_L computed for all qualified stations with a minimum of seven qualified stations. We have estimated M_L for 3,389 earthquakes, obtaining a magnitude of completeness of 1.1 and a *b*-value of 0.87 (Figure S5 in Supporting Information S1) (Goebel et al., 2017).

4. Results

The relocated catalog of events shows that most of the seismicity is located along D1 and D2 with an off-fault cluster 19 km north of D2 (Figure 2a). Seismicity along D2 aligns well with the surface fault trace, but seismicity along D1 does not match the fault trace very well due to the sparse station coverage. Seismicity on the eastern half of D1 may have also been missed for similar reasons. Thus, we restrict our interpretation of physical processes along D2 and the off-fault cluster, and do not discuss events along the D1 strand.

The seismicity shows a spatially varying pattern along the ~45 km-long D2 strand of the Discovery transform fault. The fault trace of D2 bends slightly between 20 and 25 km along strike and is misaligned with the spreading direction (Figure 2a). The seismicity follows the surface fault trace with few events observed at the ridge or inter-transform spreading center. Most of the D2 seismicity is at depths between 4 and 8 km, while shallow seismicity (<4 km) appears near the ridge-transform intersection on the western end (Figure 2b).

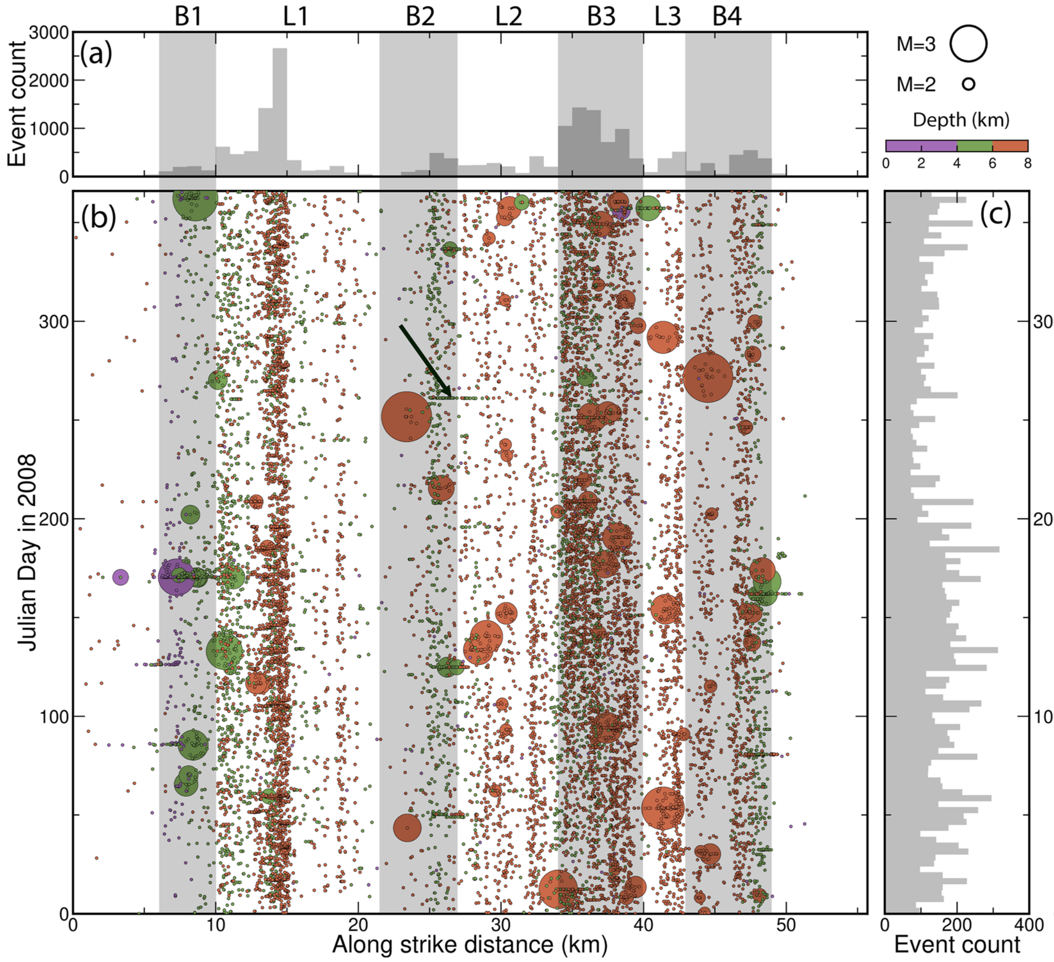

Figure 3. (a) Histogram of earthquake count along D2. B1 to B4 and L1 to L3 denote the alteration of barrier and locked zones along D2, with the gray shaded areas indicating the barrier zones. (b) Spatio-temporal and magnitude distributions of seismicity on D2. Circles are earthquakes, colored by depth and scaled by magnitude for events $M \geq 2$; gray shaded areas denote the barrier zones. Black arrow shows the seismicity triggered by the M6 earthquake on Gofar. (c) Histogram of earthquake counts with a bin length of 3 days in 2008 along D2.

Microearthquake density seems to vary along strike with alternating dense and sparse patches. Two particularly dense patches are located between 13–15 and 34–40 km along strike (Figure 3a). The former has intense seismicity at depths between 6 and 8 km, and the latter has one cluster at depths between 4 and 5 km and another one at depths between 5 and 7 km (Figures 2 and 3). A patch of sparse seismicity is found between 15 and 23 km along strike among which the segment between 20 and 23 km has few earthquakes, suggesting a possible seismicity gap (Figure 2).

The fault patches all seem to have continuous seismicity without strong temporal variations (Figure 3). A few seismicity bursts are observed near the fault-ridge intersection, often as mainshock-aftershock sequences. The largest earthquake that was observed at D2 during the experiment had a magnitude of 3.2 (Figure 3). The dense seismicity patch between 13 and 15 km and the sparse seismicity patch between 15 and 23 km lacked $M > 2$ events, while the dense seismicity patch between 34 and 40 km frequently had $M > 2$ events. A notable seismicity burst occurred on Julian day 262 of 2008 between 25 and 30 km along strike, likely dynamically triggered by the *M*6 event at the westernmost Gofar transform fault (G3; McGuire et al., 2012).

An off-fault seismicity cluster with 166 earthquakes is located about ~19 km north of D2 at 3.83°S/104.35°W (Figures 2 and 4). This cluster is aligned parallel with nearby abyssal hills and most of the events are likely at 2–4 km depth, albeit with depths less well constrained. Horizontal location of the cluster is robust, which is confirmed by *S-P* travel times from three nearby OBS stations (Figure 4a). Seismicity of the cluster continued

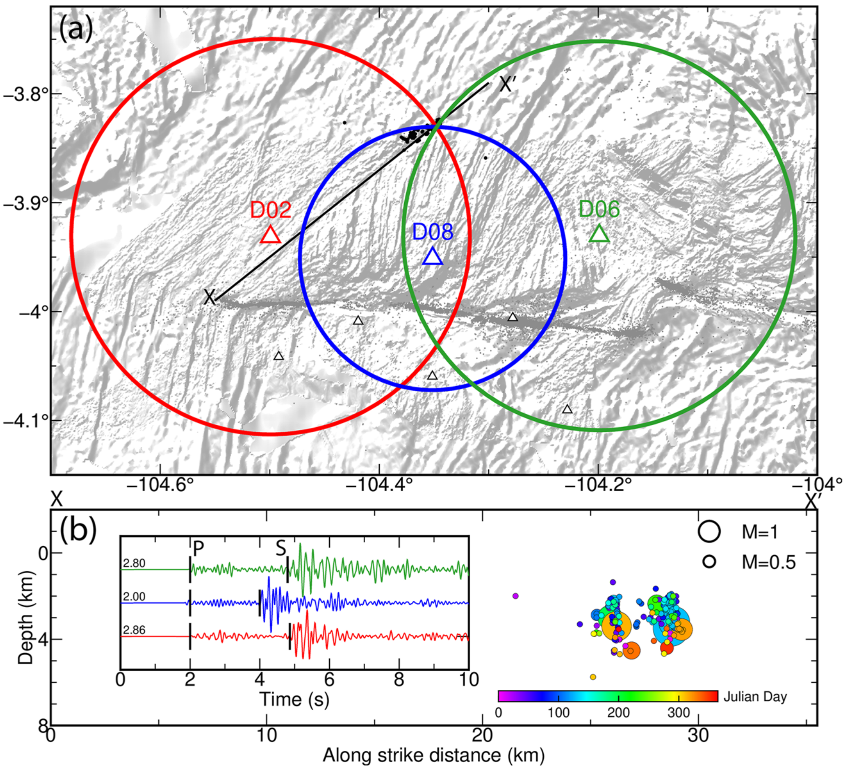

Figure 4. Off-fault seismicity cluster. (a) Confirmation of off-fault seismicity cluster location based on *S-P* travel time differences of earthquakes within the off-fault seismicity cluster measured on three ocean bottom seismometer (OBS) stations. Red, blue and green triangles denote locations of station D02, D08, and D06 respectively. Red, blue and green circles denote potential earthquake locations based on the *S-P* measurements of D02, D08, and D06, respectively. Three circles intersect at the location of the off-fault seismicity cluster. Black dots denote seismicity of the off-fault cluster. White triangles denote other OBS stations. Black line X-X′ denotes the location of the depth profile in (b). (b) Depth profile of earthquakes in the off-fault cluster. Color denotes earthquake occurrence time. Earthquakes with magnitude estimates have circle sizes scaling with their magnitudes. Insert shows vertical component waveforms from one event within the off-fault cluster. Green, blue and red traces are waveforms recorded on station D06, D08, and D02, respectively. *P* and *S* arrivals are denoted by short vertical lines. *S-P* travel time differences are shown at the beginning of each trace in seconds.

throughout the OBS deployment, and a seismicity burst occurred within this cluster on Julian Day 129 of 2008, with the largest magnitude event ($M1.5$) occurring in the middle of the sequence.

5. Discussion

5.1. Comparison With Previous Results

Our study provides refined earthquake locations at the Discovery transform fault, which confirm the general features found in Wolfson-Schwehr et al. (2014), particularly the along-strike seismicity segmentation patterns. For example, a seismicity gap at ∼104.4°W is observed in both studies. In contrast with previous studies, we find that most of the earthquakes are located at depths between 4 and 8 km, except for those near the fault-ridge intersections. It is possible that the machine-learning phase picker, PhaseNet, is more effective and robust in identifying seismic phases using OBS data than the conventional STA/LTA method used in Wolfson-Schwehr et al. (2014), which improves the subsequent location and relocation results.

5.2. Fault Segmentation at D2

The uneven and high relief bathymetry of the D2 fault includes alternating valleys and along-transform ridges (Figure 1). Seismicity density changes correlate with these valleys and ridges (Figure 1). For example, the seismicity gap between 23 and 25 km corresponds to the deepest section of the western valley and the dense seismicity patch between 34 and 40 km is located beneath an along-transform ridge (Figure 1 and Figure S6 in Supporting Information S1). These valleys and ridges might have been formed as the local tectonic system evolves, affecting regional stress field and causing fault segmentation into distinct patches (Dewey et al., 1998; Gregg et al., 2006; Grevemeyer et al., 2021; Ren et al., 2023).

The D2 fault regularly experienced $M_w > 5.4$ events over the past three decades (Wolfson-Schwehr et al., 2014). These characteristic earthquakes cluster into three discrete patches, suggesting three locked patches that rupture repeatedly along the fault (Figure 6; Wolfson-Schwehr et al., 2014; Shi et al., 2021). The $M_w > 5.4$ events on nearby locked patches tend to form doublets occurring shortly after each other instead of a single continuous rupture (Table S3 in Supporting Information S1), indicating persistent barriers between the locked patches.

We infer that the characteristic $M_w > 5.4$ events occur at three segments from west to east and denote them as L1, L2, and L3 (Figures 2 and 3), which correspond to DW1, DW2, and DW3 in Wolfson-Schwehr et al. (2014). The maximum earthquake magnitude decreases from L1 to L3 (Table S3 in Supporting Information S1, Figure 6), which may indicate reduced segment lengths (Figure 2). We assign a characteristic length of 12, 7, and 3 km for L1, L2, and L3, respectively based on the characteristic earthquakes as well as the seismicity patterns. Seismicity at these locked segments is sparse between 0 and 5.5 km depth and majority of the seismicity is deeper than 6 km, likely contouring around the locked patches above (Figure 2). The three locked patches, L1–L3, have a static westward shift of approximately 7 km compared to the DW1–DW3 locations in Wolfson-Schwehr et al. (2014) (Figure S6 in Supporting Information S1). The DW1–DW3 segmentation was inferred from the locations of $M > 5$ events at D2, which were obtained using teleseismic surface waves and their relative locations were refined using surface wave cross correlations (McGuire, 2008; Wolfson-Schwehr et al., 2014). These earthquake locations can have high accuracy in relative distances, but their absolute locations may be systematically biased up to a few kilometers (e.g., Figure 6; Shi et al., 2021).

We infer the remaining four patches, which include the two patches between L1 to L3 and the other two at the two ends of D2, as seismicity barriers. These four patches (named B1 to B4 from west to east, respectively) lack $M > 5$ earthquakes and are likely dominated by aseismic slip (Wolfson-Schwehr & Boettcher, 2019). Aseismic slip on these fault patches accommodates equal amounts of plate motion as the locked patches, but in the absence of notable ($M > 5$) earthquakes. Seismicity at these segments is typically shallower than in the connecting locked segments (Figure 2). The B2 barrier segment is situated in a ∼4 km-deep valley and likely extends 5.5 km along strike. Seismicity on this segment consists of two sharply contrasting sub-domains, with the western 3 km lacking seismicity while the eastern 2.5 km hosts relatively shallow microearthquakes. The B2 segment coincides with the bend of the fault trace and potentially represents a geometric barrier that could mechanically limit rupture propagation (Duan & Oglesby, 2005; Harris & Day, 1999; Oglesby, 2005). Such a barrier differs from damage zone-induced barriers at G3, the westernmost Gofar transform faults (Froment et al., 2014; Gong & Fan, 2022; Guo et al., 2018; Y. K. Liu et al., 2022; T. Liu et al., 2023; Roland et al., 2012). Additionally, the 2008 M6 Gofar earthquake may have dynamically triggered earthquakes at the eastern end of B2, indicating its sensitivity to stress perturbation likely due to local stress heterogeneity within the fault zone (DeSalvio & Fan, 2023; Fan et al., 2021). The western portion of B2 could also be part of L1 as seafloor acoustic ranging measurements indicate that this part of the fault is likely locked (McGuire & Collins, 2013). In this case, the absence of microearthquakes there may hint a different fault state than the rest of L1. The B3 barrier segments extends 6 km long, and is located at the along transform ridge (Figure 1). Seismicity at B3 is active and relatively shallow, indicting a possible damage zone-induced barrier as being observed at G3 (Gong et al., 2022; McGuire et al., 2012).

In comparison to the westernmost Gofar fault, G3, both faults exhibit alternating locked and barrier patches (Figure 5). Adjacent fault patches along both faults exhibit contrasting seismicity patterns such as seismicity density, and depth and temporal distributions (Figure 5; Gong & Fan, 2022; McGuire et al., 2012). The G3 fault is composed of five distinct segments (Gong & Fan, 2022), with locked zones hosting M6 characteristic earthquakes and barrier zones that may participate in both the nucleation and termination of characteristic earthquakes (Gong & Fan, 2022; McGuire et al., 2012). Similarly, the western Discovery fault, D2, is also likely segmented into distinct fault patches dominated by different slip modes (Figures 2 and 5). The barrier zones of G3 exhibit seismicity that extends to a shallow depth of approximately 2 km, whereas seismicity does not extend into the upper 4 km of the shallow crust at the D2 fault, suggesting possible different fault properties.

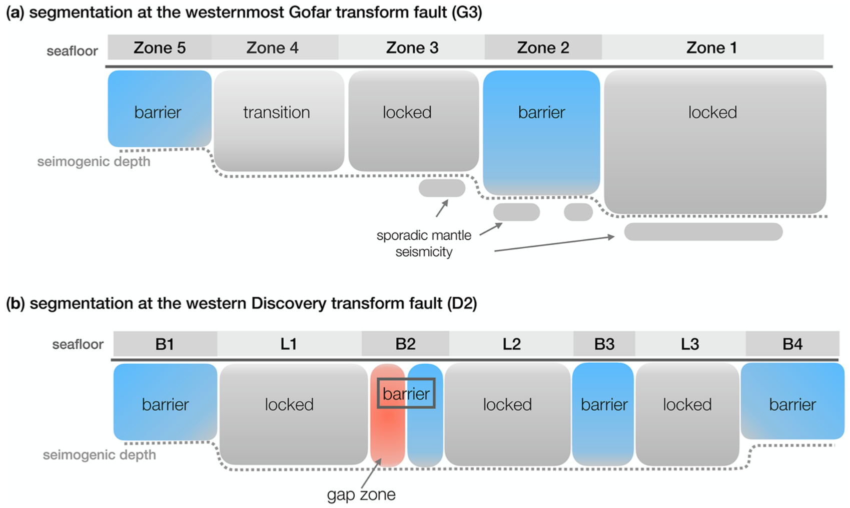

Figure 5. Conceptual cartoons of fault zone segmentation at (a) the G3 Gofar transform fault (Gong & Fan, 2022) and (b) D2 Discovery transform fault. Horizontal gray lines denote the seafloor; gray dotted lines denote seismogenic boundaries with varying depth along strike; blue and gray rounded rectangles above seismogenic depths denote locked and barrier patches of the faults; small gray rounded rectangles below seismogenic depth in (a) denote sporadic mantle seismicity patches; red rounded rectangle in (b) denotes the gap zone on D2.

5.3. Spatial Variations in Rifting Within the Discovery Transform System

The cluster of seismicity located northwest of the D2 fault indicates that there is ongoing deformation within the oceanic plate north of Discovery (Figure 6). The off-fault seismicity aligns with the orientation of a group of abyssal hills, possibly indicating reactivation of those faults. Abyssal hills are generated when seafloor spreading is accommodated by extension on normal faults, leading to scarps aligned parallel to the associated mid-ocean ridge segment where they were created (e.g., Buck & Poliakov, 1998; Macdonald et al., 1996). However, the abyssal

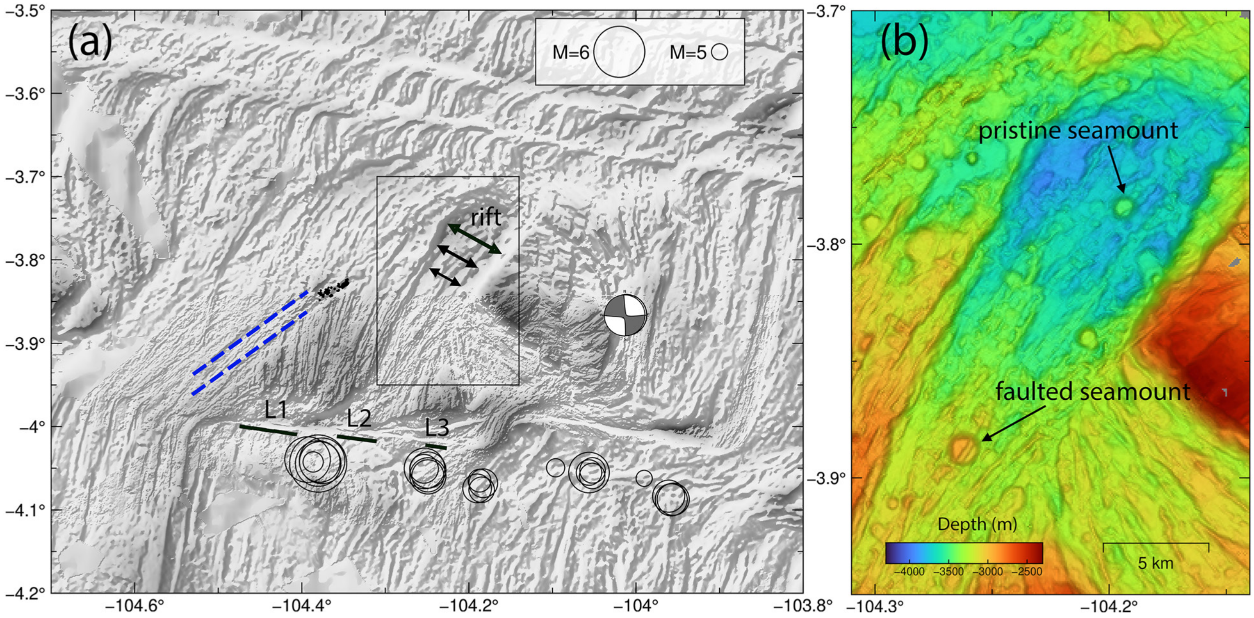

Figure 6. Regional tectonics at the Discovery transform fault system. (a) Greyscale seafloor bathymetry. Black circles denote $M \geq 5.2$ earthquakes at Discovery since 1990 (Shi et al., 2021). One strike-slip earthquake appeared to have occurred within the oceanic plate. Black dots denote earthquakes from the off-fault cluster. Double sided arrow denotes the rift zone and the decreasing rifting speed from north to south. Blue dashed lines show the orientations of the abyssal hills. Interpretations of the three locked patches, L1 to L3, are shown as short black lines. (b) Zoom-in view of the rifting zone. Two seamounts are identified in the rift zone with one pristine seamount in the north and one faulted seamount in the south.

hills north of D2 intersect with a rifting zone at an angle of 20°, suggesting possible local rotation (Figure 6). The off-fault earthquake cluster only spans a 10 km length, while the near D2 section of the abyssal hills are seismically quiescent during the deployment period, suggesting non-uniform deformation along the structure.

The approximately 10 km wide, 35 km long rift zone oriented toward N30°E suggests that there was east-west extension in the past, within the Discovery transform system. This rift zone could have served as a nascent spreading center in the past, competing with the eastern ridge. The rift zone is not parallel to the eastern ridge, and it deepens and widens from south to north. The north deepening feature indicates that the rifting process likely terminated earlier in the south than in the north, leading to varying spreading rates from south to north. This tectonic interpretation is supported by the morphology of seamounts within the rift zone. In the southern rift zone, a northeast-southwest normal fault clearly offsets a 1 km diameter seamount, suggesting brittle deformation and rifting after volcanic emplacement, while the northern seamounts are pristine (Figure 6). The southern end of the rift zone connects to D2 at the B2 barrier valley, which might be responsible for causing the fault bending and creating the B2 barrier.

The combination of off-fault seismicity and possible varying rifting rates supports the hypothesis that the off-fault earthquake cluster is situated at the latitude where rifting terminates. A spatial gradient in spreading rate could induce differential stress in the abyssal hills nearby, leading to fault reactivation and microearthquakes. Additionally, the southern termination of the rifting process may explain the seismic quiescence of the southern abyssal hills.

The seafloor morphology shows that the D2 fracture zone extends about 70 km toward the west, indicating that the Discovery faults were formed approximately 1 Myr ago, assuming a half-spreading rate of 70 mm/yr. In comparison, the Gofar and Quebrada systems are about 8 Myr old (Goff & Cochran, 1996). The reconfiguration of local tectonics may have resulted in a lack of plate spreading north of Discovery, and the rift zone may have been created to compensate for the spreading deficiency. The sequence of tectonic events has left imprints in the rift zone with varying spreading rates from south to north, local volcanism, and possible crustal block rotations (Pickle et al., 2009; Wolfson-Schwehr et al., 2014). The observed on- and off-fault seismicity may reflect local deformation in response to the tectonic activities within the Discovery transform faults.

6. Conclusions

We located and relocated 21,391 seismic events at the Discovery transform fault system using data from a 1-year long OBS deployment. Seismicity is mainly distributed along the D1 and D2 faults, and the D2 fault is likely divided into seven segments with three locked patches separated by two barrier zones. In addition, we observe an off-fault cluster of seismicity north of D2, coinciding with a group of abyssal hills. These spatial relations suggest ongoing deformation within the oceanic plate, possibly due to varying rifting rates within the Discovery system. The location of the off-fault seismicity may correspond to the latitude where rifting terminates. These observations suggest that the transform faults and surrounding oceanic plates of Discovery are still evolving, indicating a young OTF system. The Discovery transform system shows similarity and dissimilarity in seismogenic properties with the adjacent Gofar and Quebrada systems. The diverse system behaviors indicate that OTF might appear as simple tectonic systems, but they could be strongly influenced by local rifting and rotation, forming dynamic, interactive tectonic systems with complex deformation patterns.

Data Availability Statement

The seismic data are available from the Data Management Center (DMC) of the Incorporated Research Institutions for Seismology (IRIS) under the network codes ZD (http://www.fdsn.org/networks/). IRIS Data Services and the IRIS DMC were used to access waveforms, related metadata, and derived products used in this study. IRIS Data Services are funded through the Seismological Facilities for the Advancement of Geoscience and EarthScope (SAGE) proposal of the National Science Foundation (NSF) under Cooperative Agreement EAR-1261681. The relocated $M > 5.4$ events are from Shi et al. (2021), available at https://doi.org/10.5281/zenodo.4646438, and the bathymetry data can be obtained from https://www.ngdc.noaa.gov/maps/autogrid/. We used open-source software PhaseNet (Zhu & Beroza, 2018), GaMMA (Zhu et al., 2022), COMPLOC (Lin & Shearer, 2006), and GrowClust (Trugman & Shearer, 2017) for earthquake detection, association, location, and relocation, respectively. The earthquake catalog is archived at Marine Geoscience Data System (Gong et al., 2023b). Figures 1–4 and 6 are created by GMT (Wessel et al., 2019) and annotated in Adobe Photoshop. GMT bash scripts to recreate the base maps can be found at Zenodo (Gong et al., 2023a).

Acknowledgments

We thank the Editor Anne Paul, Associate Editor, and Rasheed Ajala and Milena Marjanović for their thoughtful and constructive reviews of the paper. We acknowledge support from National Science Foundation (NSF) Grant OCE-1833279 and W.F.'s startup research funds. The ocean bottom seismometer instruments were provided by the Ocean Bottom Seismograph Instrument Pool (OBSIP). The authors thank Jeffrey McGuire, John Collins, and the rest of the 2008 Quebrada–Discovery–Gofar experiment team for collecting and archiving the data.

References

Boettcher, M. S., & Jordan, T. H. (2004). Earthquake scaling relations for mid-ocean ridge transform faults. *Journal of Geophysical Research*, *109*(B12), B12302. https://doi.org/10.1029/2004JB003110

Buck, W. R., & Poliakov, A. N. B. (1998). Abyssal hills formed by stretching oceanic lithosphere. *Nature*, *392*(6673), 272–275. https://doi.org/10.1038/32636

DeMets, C., Gordon, R. G., & Argus, D. F. (2010). Geologically current plate motions. *Geophysical Journal International*, *181*(1), 1–80. https://doi.org/10.1111/j.1365-246X.2009.04491.x

DeSalvio, N. D., & Fan, W. (2023). Ubiquitous earthquake dynamic triggering in Southern California. *Journal of Geophysical Research: Solid Earth*, *128*(6), e2023JB026487. https://doi.org/10.1029/2023JB026487

Dewey, J. F., Holdsworth, R. E., & Strachan, R. A. (1998). Transpression and transtension zones. *Geological Society, London, Special Publications*, *135*(1), 1–14. https://doi.org/10.1144/GSL.SP.1998.135.01.01

Duan, B., & Oglesby, D. D. (2005). Multicycle dynamics of nonplanar strike-slip faults. *Journal of Geophysical Research*, *110*(B3), B03304. https://doi.org/10.1029/2004JB003298

Dunn, R. (2015). 1.13—Crust and lithospheric structure—Seismic structure of mid-ocean ridges. In G. Schubert (Ed.), *Treatise on geophysics* (2nd ed., pp. 419–451). Elsevier. https://doi.org/10.1016/B978-0-444-53802-4.00011-7

Fan, W., Barbour, A. J., Cochran, E. S., & Lin, G. (2021). Characteristics of frequent dynamic triggering of microearthquakes in Southern California. *Journal of Geophysical Research: Solid Earth*, *126*(1), e2020JB020820. https://doi.org/10.1029/2020jb020820

Froment, B., McGuire, J. J., van der Hilst, R. D., Gouédard, P., Roland, E. C., Zhang, H., & Collins, J. A. (2014). Imaging along-strike variations in mechanical properties of the Gofar transform fault, East Pacific Rise. *Journal of Geophysical Research: Solid Earth*, *119*(9), 7175–7194. https://doi.org/10.1002/2014JB011270

Goebel, T. H., Kwiatek, G., Becker, T. W., Brodsky, E. E., & Dresen, G. (2017). What allows seismic events to grow big? Insights from b-value and fault roughness analysis in laboratory stick-slip experiments. *Geology*, *45*(9), 815–818. https://doi.org/10.1130/G39147.1

Goff, J. A., & Cochran, J. R. (1996). The Bauer scarp ridge jump: A complex tectonic sequence revealed in satellite altimetry. *Earth and Planetary Science Letters*, *141*(1), 21–33. https://doi.org/10.1016/0012-821X(96)00061-1

Gong, J., & Fan, W. (2022). Seismicity, fault architecture, and slip mode of the westernmost Gofar transform fault. *Journal of Geophysical Research: Solid Earth*, *127*(11), e2022JB024918. https://doi.org/10.1029/2022JB024918

Gong, J., Fan, W., & Parnell-Turner, R. (2022). Microseismicity indicates atypical small-scale plate rotation at the Quebrada transform fault system, East Pacific Rise. *Geophysical Research Letters*, *49*(3), e2021GL097000. https://doi.org/10.1029/2021GL097000

Gong, J., Fan, W., & Parnell-Turner, R. (2023a). GMT bash scrips and dataset for reproducing figures in paper "Machine learning-based new earthquake catalog illuminates on-fault and off-fault seismicity patterns at the Discovery Transform Fault, East Pacific Rise" [Software]. Zenodo. https://doi.org/10.5281/zenodo.8176222

Gong, J., Fan, W., & Parnell-Turner, R. (2023b). Microseismicity catalog of Discovery transform fault, East Pacific Rise, 2008 [Dataset]. Interdisciplinary Earth Data Alliance (IEDA). https://doi.org/10.26022/IEDA/331304

Gregg, P. M., Lin, J., & Smith, D. K. (2006). Segmentation of transform systems on the East Pacific Rise: Implications for earthquake processes at fast-slipping oceanic transform faults. *Geology*, *34*(4), 289–292. https://doi.org/10.1130/g22212.1

Grevemeyer, I., Rüpke, L. H., Morgan, J. P., Iyer, K., & Devey, C. W. (2021). Extensional tectonics and two-stage crustal accretion at oceanic transform faults. *Nature*, *591*(7850), 402–407. https://doi.org/10.1038/s41586-021-03278-9

Guo, H., Zhang, H., & Froment, B. (2018). Structural control on earthquake behaviors revealed by high-resolution Vp/Vs imaging along the Gofar transform fault, East Pacific Rise. *Earth and Planetary Science Letters*, *499*, 243–255. https://doi.org/10.1016/j.epsl.2018.07.037

Harris, R. A., & Day, S. M. (1999). Dynamic 3D simulations of earthquakes on En Echelon faults. *Geophysical Research Letters*, *26*(14), 2089–2092. https://doi.org/10.1029/1999GL900377

Kohli, A. H., Wolfson-Schwehr, M., Prigent, C., & Warren, J. M. (2021). Oceanic transform fault seismicity and slip mode influenced by seawater infiltration. *Nature Geoscience*, *14*(8), 606–611. https://doi.org/10.1038/s41561-021-00778-1

Kuna, V. M., Nábělek, J. L., & Braunmiller, J. (2019). Mode of slip and crust–mantle interaction at oceanic transform faults. *Nature Geoscience*, *12*(2), 138–142. https://doi.org/10.1038/s41561-018-0287-1

Lin, G., & Shearer, P. (2006). The COMPLOC earthquake location package. *Seismological Research Letters*, *77*(4), 440–444. https://doi.org/10.1785/gssrl.77.4.440

Liu, T., Gong, J., Fan, W., & Lin, G. (2023). In-situ Vp/Vs reveals fault-zone material variation at the westernmost Gofar transform fault, East Pacific Rise. *Journal of Geophysical Research: Solid Earth*, *128*(3), e2022JB025310. https://doi.org/10.1029/2022JB025310

Liu, Y., McGuire, J. J., & Behn, M. D. (2020). Aseismic transient slip on the Gofar transform fault, East Pacific Rise. *Proceedings of the National Academy of Sciences*, *117*(19), 10188–10194. https://doi.org/10.1073/pnas.1913625117

Liu, Y. K., Ross, Z. E., Cochran, E. S., & Lapusta, N. (2022). A unified perspective of seismicity and fault coupling along the San Andreas Fault. *Science Advances*, *8*(8), eabk1167. https://doi.org/10.1126/sciadv.abk1167

Macdonald, K. C., Fox, P. J., Alexander, R. T., Pockalny, R., & Gente, P. (1996). Volcanic growth faults and the origin of Pacific abyssal hills. *Nature*, *380*(6570), 125–129. https://doi.org/10.1038/380125a0

Mammerickx, J., Anderson, R. N., Menard, H. W., & Smith, S. M. (1975). Morphology and tectonic evolution of the East-Central Pacific. *GSA Bulletin*, *86*(1), 111–118. https://doi.org/10.1130/0016-7606(1975)86⟨111:MATEOT⟩2.0.CO;2

Matoza, R. S., Shearer, P. M., Lin, G., Wolfe, C. J., & Okubo, P. G. (2013). Systematic relocation of seismicity on Hawaii Island from 1992 to 2009 using waveform cross correlation and cluster analysis. *Journal of Geophysical Research: Solid Earth*, *118*(5), 2275–2288. https://doi.org/10.1002/jgrb.50189

McGuire, J. J. (2008). Seismic cycles and earthquake predictability on East Pacific Rise transform faults. *Bulletin of the Seismological Society of America*, *98*(3), 1067–1084. https://doi.org/10.1785/0120070154

McGuire, J. J., & Collins, J. A. (2013). Millimeter-level precision in a seafloor geodesy experiment at the Discovery transform fault, East Pacific Rise. *Geochemistry, Geophysics, Geosystems*, *14*(10), 4392–4402. https://doi.org/10.1002/ggge.20225

McGuire, J. J., Collins, J. A., Gouédard, P., Roland, E., Lizarralde, D., Boettcher, M. S., et al. (2012). Variations in earthquake rupture properties along the Gofar transform fault, East Pacific Rise. *Nature Geoscience*, *5*(5), 336–341. https://doi.org/10.1038/ngeo1454

Mousavi, S. M., Ellsworth, W. L., Zhu, W., Chuang, L. Y., & Beroza, G. C. (2020). Earthquake transformer—An attentive deep-learning model for simultaneous earthquake detection and phase picking. *Nature Communications*, *11*(1), 3952. https://doi.org/10.1038/s41467-020-17591-w

Oglesby, D. D. (2005). The dynamics of strike-slip step-overs with linking dip-slip faults. *Bulletin of the Seismological Society of America*, *95*(5), 1604–1622. https://doi.org/10.1785/0120050058

Pickle, R. C., Forsyth, D. W., Harmon, N., Nagle, A. N., & Saal, A. (2009). Thermo-mechanical control of axial topography of intra-transform spreading centers. *Earth and Planetary Science Letters*, *284*(3), 343–351. https://doi.org/10.1016/j.epsl.2009.05.004

Ren, Y., Lange, D., & Grevemeyer, I. (2023). Seismotectonics of the Blanco transform fault system, Northeast Pacific: Evidence for an immature plate boundary. *Journal of Geophysical Research: Solid Earth*, *128*(3), e2022JB026045. https://doi.org/10.1029/2022JB026045

Roland, E., Lizarralde, D., McGuire, J. J., & Collins, J. A. (2012). Seismic velocity constraints on the material properties that control earthquake behavior at the Quebrada-Discovery-Gofar transform faults, East Pacific Rise. *Journal of Geophysical Research*, *117*(B11). https://doi.org/10.1029/2012JB009422

Searle, R. C. (1983). Multiple, closely spaced transform faults in fast-slipping fracture zones. *Geology*, *11*(10), 607–610. https://doi.org/10.1130/0091-7613(1983)11<607:MCSTFI>2.0.CO;2

Searle, R. C., Francis, T. J. G., Hilde, T. W. C., Somers, M. L., Revie, J., Jacobs, C. L., et al. (1981). 'Gloria' side-scan sonar in the East Pacific. *Eos, Transactions American Geophysical Union*, *62*(12), 121–122. https://doi.org/10.1029/EO062i012p00121

Shearer, P. (2019). *Introduction to seismology*. Cambridge university Press.

Shi, P., Wei, M. M., & Pockalny, R. A. (2021). The ubiquitous creeping segments on oceanic transform faults. *Geology*, *50*(2), 199–204. https://doi.org/10.1130/G49562.1

Trugman, D. T., & Shearer, P. M. (2017). GrowClust: A hierarchical clustering algorithm for relative earthquake relocation, with application to the Spanish Springs and Sheldon, Nevada, earthquake sequences. *Seismological Research Letters*, *88*(2A), 379–391. https://doi.org/10.1785/0220160188

Wessel, P., Luis, J. F., Uieda, L., Scharroo, R., Wobbe, F., Smith, W. H. F., & Tian, D. (2019). The generic mapping tools version 6. *Geochemistry, Geophysics, Geosystems*, *20*(11), 5556–5564. https://doi.org/10.1029/2019GC008515

Wolfson-Schwehr, M., & Boettcher, M. S. (2019). Global characteristics of oceanic transform fault structure and seismicity. In J. C. Duarte (Ed.), *Transform plate boundaries and fracture zones* (pp. 21–59). Elsevier.

Wolfson-Schwehr, M., Boettcher, M. S., McGuire, J. J., & Collins, J. A. (2014). The relationship between seismicity and fault structure on the Discovery transform fault, East Pacific Rise. *Geochemistry, Geophysics, Geosystems*, *15*(9), 3698–3712. https://doi.org/10.1002/2014GC005445

Yu, Z., Singh, S. C., Gregory, E. P. M., Maia, M., Wang, Z., & Brunelli, D. (2021). Semibrittle seismic deformation in high-temperature mantle mylonite shear zone along the Romanche transform fault. *Science Advances*, *7*(15), eabf3388. https://doi.org/10.1126/sciadv.abf3388

Zhu, W., & Beroza, G. C. (2018). PhaseNet: A deep-neural-network-based seismic arrival-time picking method. *Geophysical Journal International*, *216*(1), 261–273. https://doi.org/10.1093/gji/ggy423

Zhu, W., McBrearty, I. W., Mousavi, S. M., Ellsworth, W. L., & Beroza, G. C. (2022). Earthquake phase association using a Bayesian Gaussian mixture model. *Journal of Geophysical Research: Solid Earth*, *127*(5), e2021JB023249. https://doi.org/10.1029/2021JB023249